

Pattern recognition and pharmacokinetic methods on DCE-MRI data for tumor hypoxia mapping in sarcoma

M. Venianaki^{1,2} · O. Salvetti³ · E. de Bree⁴ · T. Maris⁵ ·
A. Karantanas⁵ · E. Kontopodis² · K. Nikiforaki² ·
K. Marias²

Received: 30 March 2017 / Revised: 19 June 2017 / Accepted: 18 July 2017 /

Published online: 9 August 2017

© The Author(s) 2018. This article is an open access publication, corrected publication January/2018

Abstract The main purpose of this study is to analyze the intrinsic tumor physiologic characteristics in patients with sarcoma through model-free analysis of dynamic contrast enhanced MR imaging data (DCE-MRI). Clinical data were collected from three patients with two different types of histologically proven sarcomas who underwent conventional and advanced MRI examination prior to excision. An advanced matrix factorization algorithm has been applied to the data, resulting in the identification of the principal time-signal uptake

✉ M. Venianaki
maria.venianaki@imtlucca.it

O. Salvetti
ovidio.salvetti@isti.cnr.it

E. de Bree
debree@uoc.gr

T. Maris
tmaris@med.uoc.gr

A. Karantanas
akarantanas@gmail.com

E. Kontopodis
elko@ics.forth.gr

K. Nikiforaki
kat@ics.forth.gr

K. Marias
kmarias@ics.forth.gr

¹ Image Analysis Research Unit, IMT School for Advanced Studies Lucca, Lucca, Italy

² Computational Bio-Medicine Laboratory, Institute of Computer Science, Foundation for Research and Technology – Hellas, Heraklion, Greece

curves of DCE-MRI data, which were used to characterize the physiology of the tumor area, described by three different perfusion patterns i.e. hypoxic, well-perfused and necrotic one. The performance of the algorithm was tested by applying different initialization approaches with subsequent comparison of their results. The algorithm was proven to be robust and led to the consistent segmentation of the tumor area in three regions of different perfusion, i.e. well-perfused, hypoxic and necrotic. Results from the model-free approach were compared with a widely used pharmacokinetic (PK) model revealing significant correlations.

Keywords Pattern recognition · Dynamic MR imaging · Biomedical image processing · Soft tissue sarcomas · Tumor hypoxia · Matrix factorization

1 Introduction

Hypoxia is a hallmark of most solid malignant neoplasms and is usually related with more aggressive tumor phenotypes and resistance to chemotherapy and radiotherapy [7, 15]. Tumors are associated with abnormal rapid formation of new blood vessels, in an aim to overcome the increased oxygen and other nutrient demands during tumor growth. However, tumor newly-formed vessels are typically dysfunctional impeding proper vessel-to-tissue delivery of both oxygen and chemotherapy drugs. Eventually, the augmented interstitial fluid pressure is followed by a subsequent decrease of tumor perfusion, further favoring tumor hypoxia [5]. As a result, hypoxia estimation from imaging data can play a key role in tumor characterization and lead to a more accurate and effective treatment planning.

A number of different techniques have been used for the assessment of tumor hypoxia [29]. These include invasive techniques, such as pO_2 electrode measurements and immunohistochemistry of exogenous markers e.g. pimonidazole (PIMO). Imaging techniques have also been widely used, including positron emission tomography (PET) imaging using radioactive hypoxia tracers and MR imaging. In particular, dynamic contrast enhanced MR Imaging (DCE-MRI) is a non-invasive perfusion imaging technique, which offers high spatial resolution, can be performed on clinical MRI scanners with standard specifications and can yield information concerning tissue oxygenation and vascularization. It has been used in previous studies for different purposes, such as for determining tumor grading, predicting response to therapy and differentiating between benign and malignant lesions [4, 21]. DCE-MRI involves the intravenous injection of a contrast agent (CA) with T1-weighted (w) sequences acquired before, during and after injection. The paramagnetic CA diffuses from the arteries to the extravascular extracellular space (EES), which accelerates the T1 relaxation process of tissue and leads to signal enhancement in T1-w MR images. As mentioned previously, hypoxic tumors are typically characterized by poor perfusion, thus DCE-MRI could provide useful information about the presence and distribution of hypoxia in tumors.

Currently, compartmental pharmacokinetic (PK) modeling is the most widely used technique for the DCE-MRI data analysis. It relies on dividing the anatomic area of interest in two compartments, the intravascular and EES. Perfusion related parameters are estimated in order

³ Istituto di Scienza e Tecnologie dell'Informazione "Alessandro Faedo" CNR, Area della Ricerca CNR di Pisa, Pisa, Italy

⁴ Department of Surgical Oncology, Medical School of Crete University Hospital, Heraklion, Greece

⁵ Department of Radiology, Medical School - University of Crete, Heraklion, Greece

to quantify the CA transfer rates between the different compartments and the percentage volume they occupy. However, PK models involve a number of limitations such as the signal to contrast conversion and the computationally expensive fitting algorithms [3].

A different model-free approach that has been used for the analysis of DCE-MRI data, comprises of the shape classification of the time-signal uptake curves of image voxels in a selected region of interest (ROI) within the tumor. According to the literature [12], the most common enhancement patterns of the DCE time-signal curves are three (Fig. 1). The first one is characterized by steady enhancement of the MR signal intensity (Type 1), the second one by enhancement followed by some wash-out (Type 2) and the third one by fast enhancement and rapid wash-out (Type 3). The analysis of the structure of the DCE curves is somewhat simplistic to be used for characterizing the tumor physiology. However, if combined with pattern recognition (PR) techniques, it is able to provide an automatic identification of the enhancement patterns that characterize the DCE-MRI data. Model-free and model-based methods applied on DCE-MRI data have been reviewed previously in [3].

In a previous study [2], DCE-MRI data of a rat prostate tumor were analyzed using PK modeling, resulting in the identification of well-perfused and necrotic areas, which was further validated by histology. However, PET imaging was also used for the identification of hypoxic areas. In [6, 23], DCE-MRI prostate cancer data have been analyzed using two different PR methods, nonnegative matrix factorization (NMF) and Gaussian Mixture Models (GMMs) respectively, leading to a three-area classification of the tumor in well-perfused, necrotic and hypoxic regions. The results were correlated with hypoxic areas defined by the hypoxia marker PIMO, necrotic areas defined by hematoxylin-eosin (H&E) and well-perfused areas derived from the Hoffmann pharmacokinetic model [8]. In [24], DCE pharmacokinetic parameters (k_{ep} , k^{trans} , v_e) have been compared with histopathological parameters (microvessel density parameters and tumor proliferation index) in head and neck squamous cell carcinoma (HNSCC) resulting in important correlations. In [10], the DCE parameter k_{ep} was proven to be closely correlated with VEGF expression in breast tumors. DCE-MRI parameters have been also correlated with pimonidazole and CA9 staining in patients with head-and-neck cancer [17], indicating that they can be used as

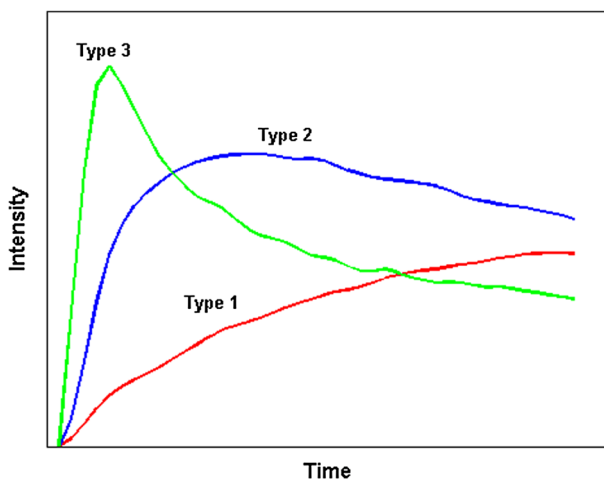


Fig. 1 The three most common shapes of tissue curves identified in various tumor types. Type 1 (red) is characterized by persistent slow enhancement of the SI while Type 2 (blue) by initial enhancement followed by some wash-out and Type 3 (green) by fast enhancement and fast wash-out

surrogate markers of hypoxia. In [31], semi-quantitative parameters of DCE-MRI were compared with H&E, PIMO and vascular endothelial growth factor (VEGF) immunohistochemistry in a maxillofacial VX2 rabbit model. Important correlations were revealed, showing that DCE-MRI is an attractive choice to offer a reliable estimation of tumor hypoxia.

Since such studies strongly indicate that DCE-MRI parameters convey hypoxia information, it is important to try to define automatic methods to extract hypoxia maps from DCE-MRI functional images. Design of a rapid and accurate image analysis algorithm for DCE-MRI data may have great impact on the evaluation of drug delivery as well as the development of specific treatments with antiangiogenic agents. To this end, herein we present a machine learning, model-free method that automatically decomposes the image in three dominant components corresponding to necrotic, hypoxic and well-perfused areas.

In particular, in this study we extended the work in [23] by applying an advanced version of the NMF algorithm and by testing it on human patient data. In particular, the block coordinate update NMF (BU-NMF) algorithm, a PR technique, was applied to DCE-MRI data derived from patients with histologically proven sarcomas. The algorithm detects the most representative patterns that comprise the data. In our previous studies [27, 28] we have examined the efficiency and robustness of this algorithm on a single patient and investigated the most suitable initialization approach to use. In the present study, the BU-NMF algorithm is tested on three patients, which have different types of sarcomas. Furthermore, in contrast to our previous reported works [27, 28], where a single slice was used, in this work information from the entire tumor volume was given as input so that the maximum available information regarding the malignancy could be used. The proposed BU-NMF-based method was applied using three different initialization approaches and the structures of the patterns identified seemed to approximate the three most common shapes of the DCE main signal-time curves (Types 1, 2 and 3), which were described previously. Well-perfused areas were defined as those having the Type 3 curve shape, hypoxic ones were assigned to the Type 2 shape and necrotic regions were those with enhancement profile similar to Type 1 curve. The classification of tumor areas has also been used in other studies investigating the role of DCE-MRI in defining hypoxia [9]. The proposed approach could be considered as a quantitative morphological analysis of the examined structures. In addition, we compare the spatial maps extracted by the PR technique with the parametric maps derived from the pharmacokinetic Extended Tofts Model (ETM), and investigate the correlation of the two different perfusion mappings for the selected tumor areas. In the k^{trans} map derived from the ETM model and for comparison purposes, image areas with high k^{trans} were labelled as well-perfused areas, those with k^{trans} zero or close to zero as necrotic areas, and those with intermediate values as hypoxic regions. Histopathology results provided by experts are also supporting, at a certain extent, the obtained results. This approach involves different types of analysis and has the advantage that by combining all the extracted information, a more global view of the tumor physiology characteristics can be obtained.

2 Materials and methods

2.1 Description of dataset

Three male patients, with median age 58 years, were included in the study. All of them were diagnosed with sarcomas, and more specifically one lower limb malignant peripheral nerve sheath tumor (MPNST), one thigh pleomorphic liposarcoma and one neck pleomorphic liposarcoma. This paper refers to the lower limb MPNST patient as Patient #1 while the patient with thigh

pleomorphic liposarcoma is mentioned as Patient #2 and the patient with neck pleomorphic liposarcoma as Patient #3. All data were provided anonymously by the University Hospital of Heraklion (Pa.G.N.I.). The patients underwent conventional and advanced MRI prior to excision. The DCE-MRI experiments were performed on a 1.5 T Siemens scanner using the contrast agent gadopentetate dimeglumine (Gd-DTPA) at routinely used dose. For the acquisition of T1-w MRI sequences, six separate acquisitions were made prior to the CA injection, with variable flip angles (VFA) of 5°, 10°, 15°, 20°, 30° and 60°. T1-w MR images were acquired with fast three-dimensional spoiled gradient echo (SPGR) with the following parameters: TR = 7 ms, TE = 3.23 ms, flip angle = 15°, voxel size 1.04 × 1.65 × 5 mm for Patient #1 and Patient #3 and 1.15 × 1.82 × 5 mm for Patient #2, acquisition matrix 192 × 121, number of slices = 14, 45 time points for DCE-MRI protocol and temporal resolution 6.44 s. DCE datasets were co-registered to the arterial phase (maximum signal-to-noise ratio (SNR)).

2.2 Pharmacokinetic model approach

The PK model used in our analysis is the ETM, which is a modified version of the well-known Tofts model (TM) [26]. TM produces reliable results only when the tissue is weakly vascularized, whereas the ETM can also be applied to highly perfused tumors [22]. The contrast agent leaves the plasma space and enters the EES at a rate represented by k^{trans} and returns by $k_{\text{ep}} = k^{\text{trans}}/v_e$, which is the exchange rate from EES to the plasma space where v_e is the volume of EES. Both k^{trans} and k_{ep} are measured in [min⁻¹]. In this study, the arterial input function (AIF) was calculated from a large vessel within the region of imaging and for the signal to contrast conversion, the method of variable flip angles (VFA) was applied. The parametric map of the k^{trans} rate was used not only for the initialization of the PR approach but also for comparing the results of the PR method with the results of the PK model method.

2.3 Pattern recognition approach

Images often contain redundant information since adjacent pixels in an image are highly correlated. To this end, dimensionality reduction algorithms are typically used to extract the important information from the image, while incurring very little error. Matrix factorization and principal component analysis are among the most popular methods for data representation in a lower-rank space. NMF, due to its non-negativity constraints, is distinguished from other matrix factorization methods such as principal component analysis (PCA). NMF results have more obvious visual interpretation and since it allows only additive combinations, it is suitable for uniting parts to generate a whole, leading to parts-based representations [13]. In our work, we want to identify certain patterns associated with cancer physiology and NMF learns to represent our MRI data as a linear combination of basis images, called patterns, each of them carrying a different weight. In this way, we can identify the pattern followed by each voxel as well as the contribution of the other patterns to each voxel of the image. This allows for a visual representation, which qualitatively resembles the nature of cancer behavior.

The basic NMF problem consists in finding an approximate decomposition of a large dimension data matrix A of size $m \times n$ into two low-rank nonnegative matrices, $m \times k$ matrix W and $k \times n$ matrix H . The ultimate aim is to minimize the functional:

$$\min_{W,H} f(W, H) = \frac{1}{2} \|A - WH\|_F^2, \text{ subject to } W, H \geq 0 \quad (1)$$

The value of k is usually selected such that $k \ll \min(m, n)$ which confirms the fact that the product WH , named the NMF of matrix A , equivalent to a compressed form of A . In practice, it corresponds to the number of basic patterns that NMF is going to use in order to represent the data in A .

The minimization of Eq. (1) involves some significant challenges. It implies the lack of convexity in both W and H , thus the existence of local minima. In addition, there is no unique solution of the minimization problem in Eq. (1) since the solution matrices W and H could also be replaced by an infinite number of other solution pairs, such as WS and $S^{-1}H$ for any nonnegative invertible matrix S having a nonnegative inverse S^{-1} .

The NMF problem has been approached by several numerical methods resulting in different solutions [1]. Lee and Seung [14] established the first well-known NMF algorithm that is based on multiplicative update rules in order to minimize the Euclidean distance described in Eq. (1). Particularly, it can be shown that the square Euclidean distance measure used in Eq. (1) is nonincreasing under the iterative updated rules described in Algorithm 1, which is presented below [1].

Algorithm 1 – Multiplicative update

```

W = rand(m, k); % initialize W as random dense matrix
H = rand(k, n); % initialize H as random dense matrix
for i = 1: maxiter
H = H. * (WTA)/(WTWH + 10-9);
W = W. * (AHT)/(WHHT + 10-9);
end

```

Alternating least squares (ALS) algorithms [18] are significantly faster to converge with respect to the multiplicative update algorithms and are based on the fact that while the minimization problem in Eq. (1) is not convex in both W and H , it is convex in either W or H . The update rules used are presented in Algorithm 2 [1].

Algorithm 2 – Alternating least squares

```

W = rand(m, k); % initialize W as random dense matrix or use another initialization
for i = 1: maxiter
(LS) Solve for H in matrix equation WTWH = WTA.
(NONNEG) Set all negative elements in H to 0.
(LS) Solve for W in matrix equation HHTWT = HAT.
(NONNEG) Set all negative elements in W to 0.
end

```

In our work, we opted for the BU-NMF algorithm, which is an efficient algorithm with simple update steps and offering global convergence under certain assumptions [30]. It relies on regularized multi-convex optimization, which is a method used in problems characterized by non-convexity and non-smoothness.

A set of points is called block multiconvex if its projection to each block of variables is convex but can be generally nonconvex. We consider a variable x , which consists of s blocks (x_1, \dots, x_s) , a set X that is a closed and block multiconvex subset of \mathbb{R}^n , f is a differentiable and block multiconvex function, and (r_1, \dots, r_s) are extended value convex functions. The optimization problem is described by the following equation [30]:

$$\min_{x \in X} F(x_1, \dots, x_s) = f(x_1, \dots, x_s) + \sum_{i=1}^s r_i(x_i) \quad (2)$$

Below it is presented the BU-NMF algorithm we used for our analysis by choosing one of the three proposed choices of update schemes in [30].

Algorithm 3 – block-coordinate update method

Initialization: choose two initial points $(x_1^{-1}, \dots, x_s^{-1}) = (x_1^0, \dots, x_s^0)$

for $k = 1, 2, \dots$ **do**

for $i = 1, 2, \dots, s$ **do**

$x_i^k \leftarrow \operatorname{argmin}_{x \in X} (g_i^k, x_i - x_i^{k-1}) + \frac{L_i^{k-1}}{2} \|x_i - x_i^{k-1}\|^2 + r_i(x_i)$ (update scheme)

end for

if stopping criteria is satisfied **then**

return (x_1^k, \dots, x_s^k)

end if

end for

In the update scheme formula used in Algorithm 3, x_i^{k-1} denotes an extrapolated point, g_i^k is the block-partial gradient of f at x_i^{k-1} and L_i^{k-1} is the Lipschitz constant of ∇f_i^k .

In [30] it was shown that the BU-NMF algorithm, when tested on synthetic, hyperspectral and real image datasets, it gave faster and more accurate results compared to other algorithms, such as multiplicative update, ALS, alternating direction method (ADM) and Blockpivot.

All the numerical results presented in this work have been obtained by Matlab 8.1.0.604 (R2013a) implemented on an Intel Core 2 i7–4770 processor, 3.4 GHz with 16 GB RAM. The code for the BU-NMF algorithm was obtained from [30]. The ETM pharmacokinetic results were obtained using a dedicated software tool for DCE-MRI data analysis [11].

2.3.1 Data pre-processing

The pre-contrast phase of the MR signal was first removed from the raw signal. A small number of pre-contrast acquisitions were obtained in order to observe the effect of the CA to MR signal intensity. Afterwards, the baseline was removed in order to extract the net effect of CA uptake on the signal intensity.

Finally, the smoothing spline method was implemented in order to remove the noise from the dynamic DCE-MRI data and obtain a smoother signal. In particular, a cubic smoothing spline algorithm was applied to the data for fitting a smooth curve to the noisy MR signal. In Fig. 2, we can see the plots resulting from all the previously described pre-processing steps applied to the original intensity curve of a specific image pixel from Patient #1.

2.3.2 BU-NMF initialization

Two different approaches have been tested for the initialization of the BU-NMF algorithm:

1. **Random initialization:** The matrices W and H are typically initialized with random nonnegative values in the standard NMF algorithm as shown in the three algorithms that were formerly presented. In our case, the BU-NMF initialization relied on taking random values from the Gaussian distribution.

Random initialization of the BU-NMF algorithm was proven not to be repeatable as it gave ambiguous results when running it for multiple times [28]. For Patient #1, we ran the BU-NMF algorithm with two different random initializations and the results were completely different. We can see in Fig. 3 that BU-NMF in one case converged to a non-interpretable solution and only nine iterations were required (Fig. 3a, c). However, when the algorithm was initialized

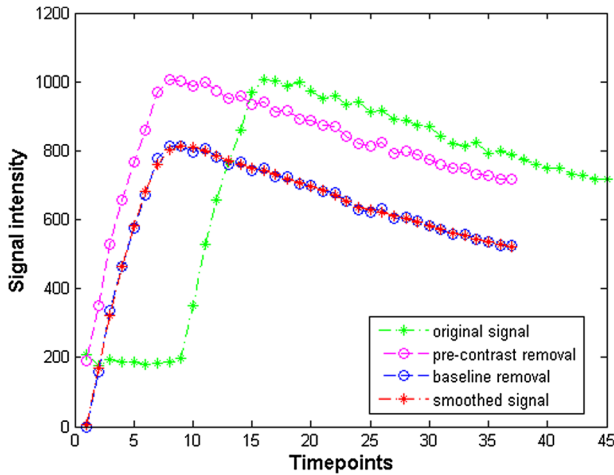


Fig. 2 Pre-processing steps applied on the intensity curve of a pixel from Patient #1. Pre-contrast phase was first removed, then the baseline, and finally smoothing was applied to the data

with different random values, it converged to interpretable results (Fig. 3b, d) and 376 iterations were required.

The number of iterations required for convergence of the BU-NMF algorithm, when ran for 50 times, is shown in Fig. 4 for all three patients. Fifty consecutive runs have been carried out by using the same ROI in each run, and different random values per voxel were produced each time for the algorithm initialization. The sets of points with the three different colors depicted in Fig. 4 correspond to each one of the three different patients.

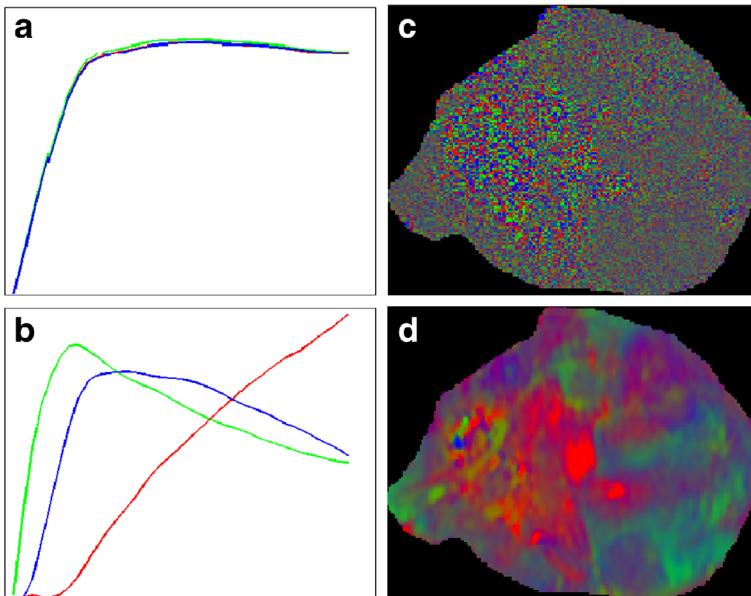


Fig. 3 BU-NMF results with the three NMF components (a, b) and the corresponding composite color maps illustrating the percentage contribution of each component (c, d) for one random initialization (a, c) and for a different random initialization (b, d)

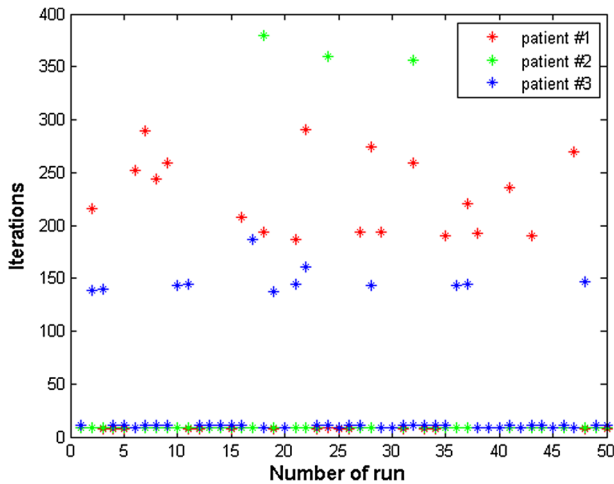


Fig. 4 Number of iterations required for the BU-NMF algorithm convergence for each of 50 consecutive runs

For all three patients, the BU-NMF algorithm sometimes converged to interpretable solutions while others it did not. As explained before for Patient #1, when it converged to a non-interpretable solution, only a few iterations were required. On the other hand, when the algorithm converged to interpretable results, a greater number of iterations were required. Therefore, we concluded that the random initialization approach did not yield reproducible results and we opted for different initialization techniques, which are explained in the following paragraphs.

2. **Data-driven initialization:** A number of such methods have also been tested, including a PK model as well as a simple gradient method. These initialization methods relied on information extracted directly from the data and when tested on the same patient data, similar results were obtained, which were also repeatable [28]. In particular, the wash-in and the k^{trans} maps were utilized for the initialization of the BU-NMF algorithm. In the first case, the BU-NMF algorithm was initialized by classifying the tumor area in three subareas using the “wash-in map” extracted from the first part of the time-signal curve related to each individual voxel. In the second initialization approach, the BU-NMF three-class initialization was derived by utilizing the k^{trans} map of ETM [26].

After computing the initial weight matrix W_0 , the H_0 matrix was initialized by the least squares solution of $A = W_0 * H_0$ where A is our given MR image data.

Concerning the decision on the value of k , for both random and data-driven initialization, PCA was applied to the data with the aim of determining the number of principal components that describe the 99% of the data variability. PCA is an orthogonal linear transformation, which projects the data onto a lower-dimensional subspace with respect to the original one. PCA involves the computation of the **covariance matrix** of the data and then its eigenvalues and corresponding eigenvectors. Eigenvectors representing the highest proportion of variance are the so-called principal components of the data. For the implementation of the PCA method, apart from the standard pre-processing reported previously, mean centering was also utilized, since this is a substantial requirement for PCA to work. After having identified the number of principal components, we used this information as an indication of how many different

patterns the BU-NMF algorithm needs to seek in order to discover the underlying patterns of the MR data.

3 Results

For all three patients, an expert clinician has annotated the tumor region of interest within the entire 3D volume of the lesion. DCE-MRI data were acquired at 45 time points and for each patient, $384 \times 384 \times 14$ pixels were used in our analysis. Data were organized in a two-dimensional data matrix $X(i, t)$, where i is an index spanning all pixels in the 3D imaging space corresponding to the selected ROI and t denotes the signal time samples. In the next paragraphs, the results from the model-driven (PK) and model-free (PR) approach are presented along with a statistical comparison between the two methods. All figures depict results from a ROI selected by an expert clinician from the central slice of malignancy for each one of the patients.

3.1 Results from the pharmacokinetic model approach

ETM was applied to the data and in particular, the biomarkers k^{trans} and k_{ep} were estimated, the extracted maps of which are shown in Fig. 5b and c for the selected central slice (Fig. 5a) of Patient #1. The k^{trans} parameter is indicative of necrotic regions [25] and necrosis is associated with no enhancement regions having zero or close to zero k^{trans} values. On the other hand, well-perfused areas are those associated with high wash-in and wash-out values corresponding to high k^{trans} and k_{ep} accordingly. Last, it is important to mention that hypoxic regions are expected to have intermediate perfusion values, therefore it is hard to identify them in a straightforward way from the PK map.

To overcome the difficulty of approximating the hypoxic regions, three-region clustering of the k^{trans} map was performed using the k-means algorithm, resulting in a better distinction between the areas having different perfusion values. The k^{trans} and clustered k^{trans} maps depicted in Fig. 6a, b respectively, were obtained from Patient #1. Areas with high perfusion were assigned to green clusters, those with moderate perfusion to blue clusters and those with low or no perfusion to red clusters.

3.2 Results from the proposed model-free pattern recognition approach

As explained in Section 2, after the data pre-processing, PCA was applied to the data in order to discover the number of components that the BU-NMF algorithm will seek. For all three

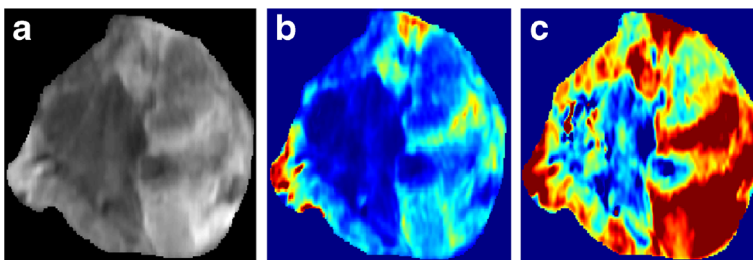


Fig. 5 Extracted maps from ETM pharmacokinetic model for Patient #1: **a)** The dynamic image. **b)** The k^{trans} map, and **c)** The k_{ep} map

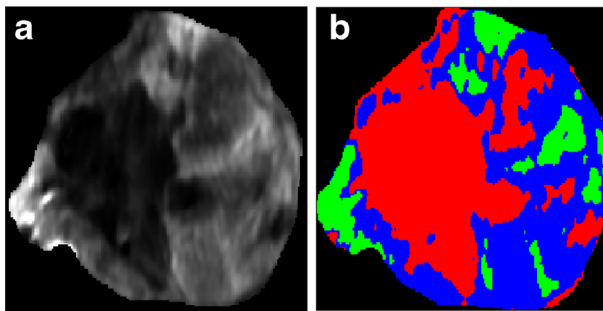


Fig. 6 Initialization of the BU-NMF algorithm using the k^{trans} parameter of ETM for Patient #1. **(a)** The k^{trans} map. **(b)** The corresponding three-area clustering using k-means, with green clusters associated with areas of high perfusion, blue clusters with moderate perfusion areas and red ones with low or no perfusion areas

patients, we found that the total data variability was sufficiently (more than 99%) described by the three first three principal components identified by PCA.

The next step concerned the implementation of the BU-NMF algorithm. The algorithm was given as prior information: a) the number of patterns that are going to represent the DCE-MRI data, which was three as shown by the PCA results, and b) the initialized W_0 and H_0 matrices using the wash-in and PK initialization method, described previously in Section 2.

3.2.1 Initialization results

The first BU-NMF initialization approach relied on the extraction of the wash-in map, described in Section 2.3.2. A three-region classification map was subsequently derived from the wash-in map using the k-means algorithm. This map is depicted in Fig. 7a and it corresponds to Patient #2. Areas with high wash-in values are colored green, those with intermediate wash-in are blue and those with low or zero wash-in values are red.

The second BU-NMF initialization approach relied on the extraction of the k^{trans} map from the ETM model, similarly to the concept mentioned in the pharmacokinetic model method (Section 3.1). The extracted map from Patient #2 is illustrated in Fig. 7b.

The two initialization maps appear quite similar in terms of the necrotic region (red) but don't seem to agree very much on the well-perfused (green) and hypoxic (blue) regions.

3.2.2 BU-NMF results

Results from both the wash-in and PK map initialization of the BU-NMF algorithm are illustrated in the following figures. In Figs. 8, 9, 10 the results from the BU-NMF implementation using wash-in initialization, are presented for Patients #1, #2 and #3 respectively. In Figs. 8a, 9a, 10a the plots of the three NMF components are depicted and in Figs. 8c, 9c, 10c the corresponding composite color maps are illustrated, showing the contribution of the three components to each individual voxel. Each image voxel is characterized by a mixture of well-perfused (green), hypoxic (blue) and necrotic (red) regions. The results of the PR analysis using the PK map initialization, containing the NMF plots and the composite color maps are shown in Figs. 8b, 9b, 10b and Figs. 8d, 9d, 10d respectively. We notice that for all three patients, the three different NMF components have the shape of the theoretically expected DCE curves as explained in Section 1, confirming the efficiency of the BU-NMF algorithm in automatically characterizing the enhancement profiles. In addition, considering the apparent

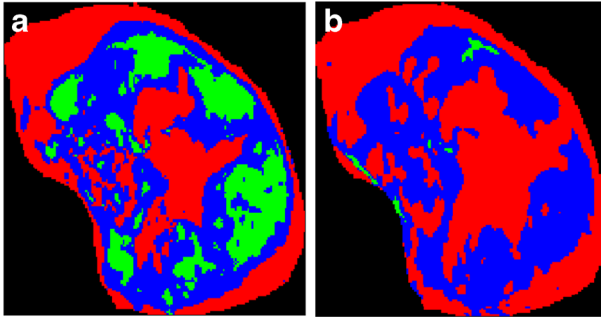


Fig. 7 Initialization of the BU-NMF algorithm using the wash-in and the PK map for Patient #2. **(a)** The three-region clustering map derived from k-means clustering on the wash-in map, with green clusters representing the high wash-in areas, blue representing the moderate wash-in areas and red ones representing the low or no wash-in areas. **(b)** The three-region clustering map derived from k-means clustering on the PK map, with green clusters representing the high perfusion areas, blue representing the moderate perfusion areas and red representing the low or no perfusion areas

high variability in the initial conditions the method in all cases yields consistent results. This is further investigated in the next section.

3.3 Statistical analysis

Statistical analysis of our results was performed using Pearson's linear correlation coefficient. The correlation coefficient can range between -1 and 1 , which we corresponded to percentages ranging from -100% and 100% . A perfect positive correlation is represented by the value $+1$, the value 0 indicates no correlation and -1 indicates a perfect negative correlation. The closer the coefficient values are to 1 and -1 , the stronger the relationship is between the variables. All image correlations described in the following paragraphs have been computed following image background removal, thus taking into account only the tumor ROI pixels.

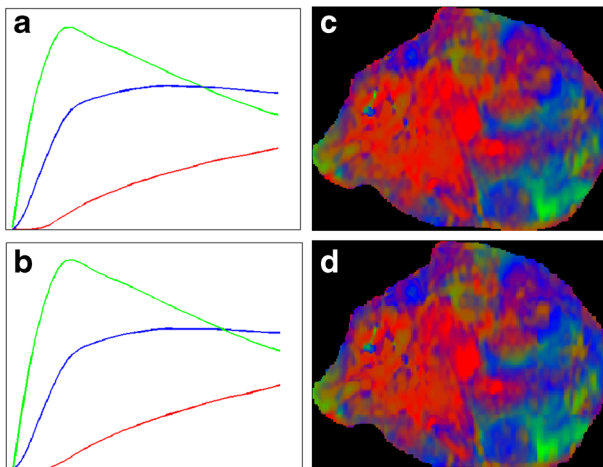


Fig. 8 PR analysis results for Patient #1. Left: Plots of the three NMF components using the wash-in map **(a)** and the PK map initialization **(b)** respectively. Right: The corresponding composite color maps **(c, d)** derived from the two different initialization approaches describing the percentage contribution of the well-perfused (green), hypoxic (blue), and necrotic (red) components

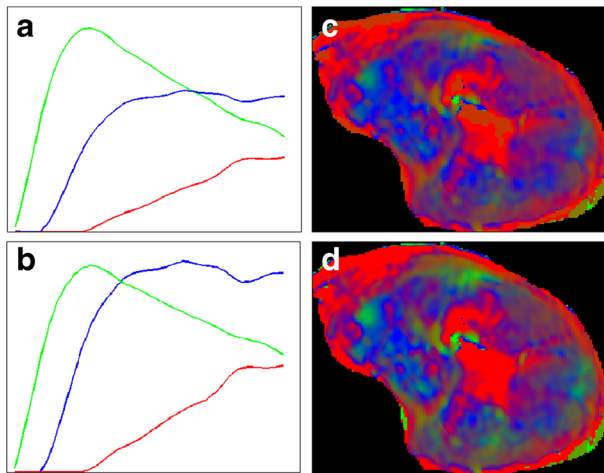


Fig. 9 PR analysis results for Patient #2. Left: Plots of the three NMF components using the wash-in map (a) and the PK map initialization (b) respectively. Right: The corresponding composite color maps (c, d) derived from the two different initialization approaches describing the percentage contribution of the well-perfused (green), hypoxic (blue), and necrotic (red) components

In order to investigate the correspondence between the hypoxic, well-perfused and necrotic components derived from the two BU-NMF initialization approaches. The results are presented in Table 1 for all three patients.

We notice that the highest correlation percentages (greater than 91%) appear when the same components from the two different BU-NMF implementations are compared e.g. hypoxic

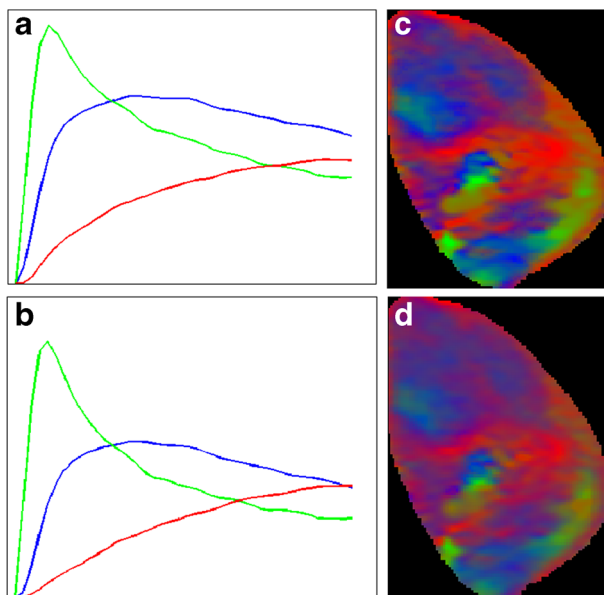


Fig. 10 PR analysis results for Patient #3. Left: Plots of the three NMF components using the wash-in map (a) and the PK map initialization (b) respectively. Right: The corresponding composite color maps (c, d) derived from the two different initialization approaches describing the percentage contribution of the well-perfused (green), hypoxic (blue), and necrotic (red) components

component from wash-in initialization with hypoxic component from PK initialization. As expected, all comparisons of different components exhibit either low or negative correlations.

The relationship between the BU-NMF classification and the k^{trans} map three-region classification using k-means clustering, as explained in Section 3.1, was also investigated and the derived correlation percentages are presented in Table 2. The BU-NMF classification results were obtained from Patient #1 using the wash-in initialization method. Similar results were obtained when the PK initialization was chosen instead. Correlation is dominant when the same regions are compared even though percentages are not as high as in Table 1, ranging between 38.44% and 66.92%. The necrotic regions show the highest correlation (66.92%) whereas well-perfused and hypoxic components show lower correlation, i.e. 45.99% and 38.44% respectively. This might be due to the fact that the k^{trans} parameter is indicative of necrotic regions, as explained in Section 3.1, but is not able to distinguish well between the well-perfused and hypoxic regions when a simple classification method as k-means is used. Negative or low correlation percentages were observed when different components from the two methods were described.

In order to get a further understanding of the extracted tumor hypoxic regions, we focused on comparing only the hypoxic map extracted from the BU-NMF algorithm with the entire k^{trans} map (Table 3). Correlation percentages varied between 23.73–43.23%, which does not give very much evidence of correlation between the two methods.

Subsequently, we applied a double thresholding technique on the k^{trans} image in order to approximate the location of the hypoxic region in the tumor. The rationale for this is that the hypoxic areas will exhibit a k^{trans} profile greater than the necrotic ($k^{\text{trans}} = 0$) but less than the well-perfused areas ($k^{\text{trans}} > 1$). We tested different threshold values and we identified the upper and lower bounds in the k^{trans} image that lead to the highest correlation between the image derived from k^{trans} thresholding and the hypoxic region derived from BU-NMF (Table 4). It is noticeable that for all three patients these bounds were between 0.15 and 0.76 approximately, with k^{trans} taking on values in a range of 0–1, leading to a maximum correlation with BU-NMF results of around 52%. From this, we could assume that the necrotic image regions according to our classification exhibit k^{trans} values lower than 0.15, well-perfused exhibit k^{trans} more than 0.76 and hypoxic regions lie in between these two thresholds. This assumption is reasonable since the hypoxic k^{trans} range is in line with findings claiming that the bulk of the tumor consists mainly of hypoxia; hence, the periphery of the tumor, which typically relates to the normoxic/well-perfused area, occupies smaller space [16, 25]. Necrotic regions instead are those with k^{trans} close to zero, occupying a smaller space with respect to hypoxia. However, in our case the necrotic region seemed to be overestimated by a small percentage of 15%, which can be explained by the limitation of MR imaging resolution regarding

Table 1 Correlation (%) between the hypoxic, well-perfused and necrotic components using the two initialization schemes for the BU-NMF algorithm

	Wash-In								
	Hypoxic			Well-Perfused			Necrotic		
	Patient #1	Patient #2	Patient #3	Patient #1	Patient #2	Patient #3	Patient #1	Patient #2	Patient #3
PK									
Hypoxic	98.09	99.64	96.37	-17.12	-12.42	-25.72	-74.59	-85.14	-76.37
Well-Perfused	-4.26	5.71	-18.92	99.79	91.11	98.83	-51.3	-49.01	-46.37
Necrotic	-87.83	-82.09	-71.37	-43.37	-45.55	-44.68	99.1	96.96	98.25

Table 2 Correlation (%) between the BU-NMF (wash-in initialized) and the k^{trans} (clustered by k-means) hypoxic, well-perfused and necrotic components for Patient #1

BU-NMF	k^{trans}		
	Hypoxic	Well-Perfused	Necrotic
Hypoxic	38.44	6.86	-42.86
Well-Perfused	23.75	45.99	-54.88
Necrotic	-0.46	-31.2	66.92

physiology, thus voxels with values close to zero that are adjacent to necrotic regions with $k^{\text{trans}} = 0$ are also considered as necrotic. Similar assumptions for the k^{trans} range were used in a recent study [19], which deals with the delineation of tumor physiological regions through the application of a cancer predictive model aiming to predict patients' glioblastoma progress.

3.4 Qualitative findings from Histopathology reports

There is consistency in the morphological characterization of the three lesions regarding the existence of necrotic areas sporadically distributed within the tumors. In addition, all three tumors have been characterized by regionally high proliferation rates.

Specifically, for the patient with MPNST sarcoma, the immunohistochemical analysis has shown positive value of the proliferation marker (MIB-1), high cellularity as well as positive values of the microvessel density parameter CD34.

We can assume that localization of regions with high cellularity and vascularization, might indicate either lack of adequate oxygenation of the tumor, hence hypoxic regions, or presence of well-perfused areas.

4 Discussion

In the present work, three different approaches were tested on DCE-MRI data obtained from patients affected by sarcoma; the quantitative pharmacokinetic ETM model, the semi-quantitative BU-NMF algorithm applied on the time-signal DCE curves and the qualitative examination of the data provided by experienced radiologists. The ETM model provided us with the k^{trans} map, which is a well-established quantitative parameter for the localization of perfusion areas. As of the semi-quantitative PR approach, the BU-NMF algorithm was initialized by one random approach and two data-driven approaches. In terms of histopathological data, important tumor morphological information was obtained and for one of the three patients immunohistochemical information was also provided.

In particular, the three most common theoretically expected types of DCE tissue curve shapes (Types 1, 2 and 3) were confirmed by the results of the BU-NMF algorithm as being the

Table 3 Correlation (%) between the k^{trans} map and the hypoxic map extracted from BU-NMF with different initialization schemes

	k^{trans} versus BU-NMF hypoxic map/Wash-in	k^{trans} versus BU-NMF hypoxic map/PK
Patient #1	32.26	23.73
Patient #2	43.23	39.36
Patient #3	38.87	40.51
Mean for all patients	38.12	34.53

Table 4 Correlation (%) between hypoxic maps extracted from the k^{trans} map and BU-NMF and corresponding k^{trans} bounds

	k^{trans} versus BU-NMF with Wash-in			k^{trans} versus BU-NMF with PK		
	Correlation (%)	k^{trans} lower bound	k^{trans} upper bound	Correlation (%)	k^{trans} lower bound	k^{trans} upper bound
Patient #1	53	0.14	0.52	48.59	0.12	0.7
Patient #2	57.7	0.06	0.77	55.82	0.05	0.77
Patient #3	50.17	0.28	0.76	48.99	0.29	0.81
Mean for all patients	53.62	0.16	0.68	51.13	0.15	0.76

dominant patterns that represent the signal. In addition, the well-perfused, hypoxic and necrotic components extracted from the two BU-NMF implementations (wash-in and PK initialized), correlated well between them while there was also a positive correlation with the same components extracted from the k^{trans} map with a simple k-means clustering. Small positive correlations were observed when comparing the k^{trans} image with the hypoxic component of BU-NMF. The correlations were significantly improved, i.e. improvement of 41% for wash-in and 48% for PK initialization, when only a constrained (via double thresholding) part of the k^{trans} map was compared against the hypoxic BU-NMF image. What is more, from the double thresholding technique we used on the k^{trans} image, the BU-NMF hypoxic regions best correlated to k^{trans} image with values between 0.15 and 0.76 approximately, well-perfused areas to k^{trans} above 0.76 and necrotic regions to k^{trans} below 0.15. These results are in agreement with published results and findings on tumor hypoxia [16, 25] as explained in Section 3.3. The histopathological findings indicated the presence of necrotic and well-perfused areas in all three lesions, however the detection of hypoxic regions would need further analysis since we only obtained immunohistochemistry results for one of the three patients.

In conclusion, the PR method used in this work gave fast (around 25 s execution time) and repeatable results, always converging after a precise number of iterations for each patient. In addition, the results obtained did not depend on complex fitting or initialization procedures in contrast to computationally expensive PK models, which also require non-linear fitting schemes that may lead to local extrema problems. After successfully addressing the problems related to random initialization, the presented method was robust to initial conditions since it gave very similar results for both initialization schemes. In addition, user interaction was minimal, whereas for PK models there is need to select certain parameters in advance such as the AIF [3]. Last but not least, in contrast to model-based approaches, our method does not make any assumptions on the underlying biology since it is purely data-driven.

The findings stemming from the present study may be useful in many different ways. Tumor classification based on hypoxia, could be very helpful in determining the malignancy grade of a tumor and most importantly in assisting the oncologist to suggest more effective treatment planning and possibly limit or even avoid the radiation therapy. Achieving hypoxia delineation and mapping of the diverse perfusion areas present in heterogeneous tumors, will be also useful in guiding core needle biopsy so that it targets the most representative areas of the tumor. In addition, it could help to differentiate tumors based on the perfusion maps extracted from the MRI examination that could play a key role in deciding whether surgery is needed or not.

An obvious limitation of the current work is further validation against histopathology and immunohistochemistry, which was not available for all three sarcomas. To this end, the current

work focused mainly on demonstrating the increased stability and invariance to initial conditions that previous work suffered [27] and on correlating the automatically extracted regions to the well-known k^{trans} variable. Interestingly, our results show that by containing the k^{trans} parametrized image with a double threshold (lower to exclude necrosis and upper to exclude well-perfused areas), the correlation to our extracted hypoxic components increases significantly. This is an encouraging indication that our data-based approach is able to produce clinically significant results related to tumor hypoxia, a hypothesis that needs further investigation in order to be confirmed.

To this end, we will also compare a large number of pharmacokinetic parameters from a wide range of DCE-MRI models such as Tofts and GCTT [20], in order to examine possible correlations more thoroughly and compare them to already published work from studies investigating the relationship of DCE-MRI to tumor hypoxia. The main plan for future work is to compare our computational results from the model-free and model-based approach with quantitative histopathological parameters. All the tissue sections analyzed computationally, will be histopathologically examined for morphological features, while additional immunohistochemistry will identify biomarkers, which will be afterwards translated to hypoxia and other related cancer hallmarks. What is more, further work and analysis on a large series of tumor image data will be performed in order to confirm our results and investigate the correlations between model-based, model-free methods and histopathology in different tumor malignancies.

5 Conclusion

The present study analyzed the tumor physiology of three histologically different sarcomas by using non-invasive DCE-MR imaging data, which were post-processed leading to quantitative and semi-quantitative results. An advanced matrix factorization algorithm, BU-NMF, has been applied to the data and its results were compared to the pharmacokinetic ETM model and to histopathology findings as well. Our results indicate that hypoxia can be estimated from non-invasive DCE-MR imaging data using purely data-driven methods.

The BU-NMF algorithm was proved to be robust, as it gave consistent results when initialized by different methods. It yielded to the identification of the three most common enhancement patterns of the DCE time-signal uptake curves, which is in line with theoretical findings claiming that there are three types of DCE tissue curves as explained in Section 1. BU-NMF also segmented the tumor area in three regions characterized by different perfusion, i.e. well-perfused, hypoxic and necrotic one, which correlated well when compared with the same areas extracted from the k^{trans} parametric map of the pharmacokinetic ETM model. Interestingly, the BU-NMF hypoxic map seems to correlate with a constrained k^{trans} image, as is theoretically expected. What is more, from the histopathological findings, the existence of necrotic and well-perfused areas in the three lesions was further confirmed.

The current study enabled us to obtain an objective evaluation of the physiology of the lesions under examination, which was supported by the qualitative analysis of the experts. Once this is validated, it could be particularly useful as an imaging hypoxia biomarker for monitoring the follow up of the patient. To this end, additional studies have been planned to test the algorithm on larger patient cohorts and to validate the results through histopathology, with the ultimate goal to develop an automated tool for the detection of hypoxia using DCE-MRI.

Acknowledgments KM acknowledges support from the CHIC project GA600841 funded by the 7th Framework Programme of the European Commission. The authors thank Mariam-Eleni Oraipoulou for helpful discussions and comments regarding tumor physiology that greatly improved the manuscript.

Open Access This article is distributed under the terms of the Creative Commons Attribution 4.0 International License (<http://creativecommons.org/licenses/by/4.0/>), which permits use, duplication, adaptation, distribution and reproduction in any medium or format, as long as you give appropriate credit to the original author(s) and the source, provide a link to the Creative Commons license, and indicate if changes were made.

References

1. Berry MW, Browne M, Langville AN, Pauca VP, Plemmons RJ (2007) Algorithms and applications for approximate nonnegative matrix factorization. *Comput Stat Data Anal* 52(1):155–173. <https://doi.org/10.1016/j.csda.2006.11.006>
2. Cho H, Ackerstaff E, Carlin S et al (2009) Noninvasive Multimodality Imaging of the Tumor Microenvironment: Registered Dynamic Magnetic Resonance Imaging and Positron Emission Tomography Studies of a Preclinical Tumor Model of Tumor Hypoxia. *Neoplasia* 11(3):247IN2–259IN3. <https://doi.org/10.1593/neo.81360>
3. Eyal E, Degani H (2009) Model-based and model-free parametric analysis of breast dynamic-contrast-enhanced MRI. *NMR Biomed* 22(1):40–53. <https://doi.org/10.1002/nbm.1221>
4. Fisher SM, Joodi R, Madhuranthakam AJ, Öz OK, Sharma R, Chhabra A (2016) Current utilities of imaging in grading musculoskeletal soft tissue sarcomas. *Eur J Radiol* 85(7):1336–1344. <https://doi.org/10.1016/j.ejrad.2016.05.003>
5. Fukumura D, Jain RK (2007) Tumor microenvironment abnormalities: Causes, consequences, and strategies to normalize. *J Cell Biochem* 101(4):937–949. <https://doi.org/10.1002/jcb.21187>
6. Han SH, Ackerstaff E, Stoyanova R et al (2013) Gaussian mixture model-based classification of dynamic contrast enhanced MRI data for identifying diverse tumor microenvironments: preliminary results. *NMR Biomed* 26(5):519–532. <https://doi.org/10.1002/nbm.2888>
7. Höckel M, Schlenger K, Mitze M, Schäffer U, Vaupel P (1996) Hypoxia and radiation response in human tumors. *Semin Radiat Oncol* 6(1):3–9. [https://doi.org/10.1016/S1053-4296\(96\)80031-2](https://doi.org/10.1016/S1053-4296(96)80031-2)
8. Hoffmann U, Brix G, Knopp MV, Heß T, Lorenz WJ (1995) Pharmacokinetic Mapping of the Breast: A New Method for Dynamic MR Mammography. *Magn Reson Med* 33(4):506–514. <https://doi.org/10.1002/mrm.1910330408>
9. Jensen RL, Mumert ML, Gillespie DL, Kinney AY, Schabel MC, Salzman KL (2014) Preoperative dynamic contrast-enhanced MRI correlates with molecular markers of hypoxia and vascularity in specific areas of intratumoral microenvironment and is predictive of patient outcome. *Neuro Oncol* 16(2):280–291. <https://doi.org/10.1093/neuonc/not148>
10. Knopp MV, Weiss E, Sinn HP et al (1999) Pathophysiologic basis of contrast enhancement in breast tumors. *J Magn Reson Imaging* 10(3):260–266. [https://doi.org/10.1002/\(SICI\)1522-2586\(199909\)10:3<260::AID-JMRI6>3.0.CO;2-7](https://doi.org/10.1002/(SICI)1522-2586(199909)10:3<260::AID-JMRI6>3.0.CO;2-7)
11. Kontopodis E, Karatzanis I, Sakkalis V, Francesca B, Marias K (2016) A DCE-MRI analysis workflow. *CGI '16: Proceedings of the 33rd Computer Graphics International conference*, 101–104. <https://doi.org/10.1145/2949035.2949061>
12. Kuhl CK, Mielcarek P, Klaschik S et al (1999) Dynamic breast MR imaging: are signal intensity time course data useful for differential diagnosis of enhancing lesions? *Radiology* 211:101–110. <https://doi.org/10.1148/radiology.211.1.r99ap38101>
13. Lee DD, Seung HS (1999) Learning the parts of objects by non-negative matrix factorization. *Nature* 401(6755):788–791. <https://doi.org/10.1038/44565>
14. Lee DD, Seung HS (2001) Algorithms for Non-negative Matrix Factorization. *Adv Neural Inf Process Syst* 13:556–562
15. Menon C, Fraker DL (2005) Tumor oxygenation status as a prognostic marker. *Cancer Lett* 221(2):225–235. <https://doi.org/10.1016/j.canlet.2004.06.029>
16. Neal ML, Trister AD, Cloke T et al (2013) Discriminating Survival Outcomes in Patients with Glioblastoma Using a Simulation-Based, Patient-Specific Response Metric. *PLoS One* 8(1):e51951. <https://doi.org/10.1371/journal.pone.0051951>
17. Newbold K, Castellano I, Charles-Edwards E et al (2009) An Exploratory Study Into the Role of Dynamic Contrast-Enhanced Magnetic Resonance Imaging or Perfusion Computed Tomography for Detection of Intratumoral Hypoxia in Head-and-Neck Cancer. *Int J Radiat Oncol Biol Phys* 74(1):29–37. <https://doi.org/10.1016/j.ijrobp.2008.07.039>
18. Paatero P, Tapper U (1994) Positive matrix factorization: A non-negative factor model with optimal utilization of error estimates of data values. *Environmetrics* 5(2):111–126. <https://doi.org/10.1002/env.3170050203>
19. Roniotis A, Oraipoulou M-E, Tzamali E et al (2015) A Proposed Paradigm Shift in Initializing Cancer Predictive Models with DCE-MRI Based PK Parameters: A Feasibility Study. *Cancer Informat* 14(Suppl 4): 7. <https://doi.org/10.4137/CIN.S19339>

20. Schabel MC (2012) A unified impulse response model for DCE-MRI. *Magn Reson Med* 68(5):1632–1646. <https://doi.org/10.1002/mrm.24162>
21. Soldatos T, Ahlawat S, Montgomery E, Chalian M, Jacobs MA, Fayad LM (2016) Multiparametric Assessment of Treatment Response in High-Grade Soft-Tissue Sarcomas with Anatomic and Functional MR Imaging Sequences. *Radiology* 278(3):831–840. <https://doi.org/10.1148/radiol.2015142463>
22. Sourbron SP, Buckley DL (2011) On the scope and interpretation of the Tofts models for DCE-MRI. *Magn Reson Med* 66(3):735–745. <https://doi.org/10.1002/mrm.22861>
23. Stoyanova R, Huang K, Sandler K et al (2012) Mapping Tumor Hypoxia In Vivo Using Pattern Recognition of Dynamic Contrast-enhanced MRI Data. *Transl Oncol* 5(6):437–IN2. <https://doi.org/10.1593/tlo.12319>
24. Surov A, Meyer HJ, Gawlitza M et al (2017) Correlations Between DCE MRI and Histopathological Parameters in Head and Neck Squamous Cell Carcinoma. *Transl Oncol* 10(1):17–21. <https://doi.org/10.1016/j.tranon.2016.10.001>
25. Swanson KR, Chakraborty G, Wang CH et al (2009) Complementary but distinct roles for MRI and 18F-fluoromisonidazole PET in the assessment of human glioblastomas. *J Nucl Med* 50(1):36–44. <https://doi.org/10.2967/jnumed.108.055467>
26. Tofts PS, Kermode AG (1991) Measurement of the blood-brain barrier permeability and leakage space using dynamic MR imaging. 1. Fundamental concepts. *Magn Reson Med* 17(2):357–367. <https://doi.org/10.1002/mrm.1910170208>
27. Venianaki M, Kontopodis E, Nikiforaki K, de Bree E, Salvetti O, Marias K (2016) A model-free approach for imaging tumor hypoxia from DCE-MRI data. CGI '16:Proceedings of the 33rd Computer Graphics International conference, 105–108. <https://doi.org/10.1145/2949035.2949062>
28. Venianaki M, Kontopodis E, Nikiforaki K, et al (2016) Improving hypoxia map estimation by using model-free classification techniques in DCE-MRI images. 2016 IEEE International Conference on Imaging Systems and Techniques (IST), 183–188. <https://doi.org/10.1109/IST.2016.7738220>
29. Walsh JC, Lebedev A, Aten E, Madsen K, Marciano L, Kolb HC (2014) The clinical importance of assessing tumor hypoxia: relationship of tumor hypoxia to prognosis and therapeutic opportunities. *Antioxid Redox Signal* 21(10):1516–1554. <https://doi.org/10.1089/ars.2013.5378>
30. Xu Y, Yin W (2013) A block coordinate descent method for regularized multiconvex optimization with applications to nonnegative tensor factorization and completion. *SIAM J Imag Sci* 6(3):1758–1789. <https://doi.org/10.1137/120887795>
31. Zheng L, Li Y, Geng F et al (2015) Using semi-quantitative dynamic contrast-enhanced magnetic resonance imaging parameters to evaluate tumor hypoxia: a preclinical feasibility study in a maxillofacial VX2 rabbit model. *Am J Transl Res* 7(3):535–547



Maria Venianaki is a PhD student in Image Analysis at IMT School for Advanced Studies Lucca. She is also a visiting fellow at the Computational BioMedicine Laboratory at FORTH-ICS since October 2016. She completed her masters in Bioengineering from Imperial College London. Her undergraduate degree was in Electrical and Computer Engineering from Aristotle University of Thessaloniki. Her current research interests include Pattern recognition and Medical image processing.



Ovidio Salvetti holds the position of Director of Research of the National Research Council of Italy (CNR) at the Institute of Information Science and Technologies (ISTI), in Pisa. He is working in the fields of theoretical and applied computer vision, multimedia, and computational intelligence. His research interests are image analysis and understanding, multimedia information systems, spatial modeling, decision support systems, and intelligent processes in computer vision. He is coauthor of seven books and monographs and more than four hundred technical and scientific articles; he is also owner of eleven patents regarding systems and software tools for image processing. Salvetti has been the Scientific Coordinator of more than 40 National and European research and industrial projects, in collaboration with Italian and foreign research groups, in the fields of computer vision, multimedia semantics, and high-performance computing for diagnostic imaging. He also worked as Vice Coordinator of the subproject Dedicated Processors of the CNR finalized program Information Systems and Parallel Computation and one of the promoters of the CNR strategic project Knowledge through Images. He is member on the editorial boards of the International Journals Pattern Recognition and Image Analysis, Forensic Computer Science, The Open Medical Informatics, Transactions on Mass-Data Analysis of Images and Signals, Transactions on Case-based Reasoning, and Atti della Fondazione “Giorgio Ronchi”. He is currently Associate Editor of IET Image Processing journal, Member of the IEEE CIS, and Head of the ISTI Signals and Images Laboratory.



Eelco de Bree is an Associate Professor of General Surgery and Surgical Oncology at the Medical School of Crete. After graduating from the Medical School of the University of Utrecht, the Netherlands, he completed his residency of General Surgery in the Medical School of Crete University Hospital in Heraklion, Greece, and became a board certified surgeon in Greece and in the Netherlands. After a 2-year fellowship at the Antoni van Leeuwenhoek Hospital / Netherlands Cancer Institute in Amsterdam, he returned to Greece in 2000. Since then, he has been an attending surgeon at the Department of Surgical Oncology of the University Hospital in Heraklion, Greece. He successfully presented his thesis entitled ‘Objective assessment of the contribution of diagnostic methods in malignant jaundice’ at the Medical School of Crete. Receiving also the certification of Surgical Oncologist in the Netherlands, he is registered as General Surgeon as well as Surgical Oncologist in the Specialist Register of the Royal Dutch Medical Association. He has published approximately 100 papers in international peer-reviewed journals and approximately 30 papers in national journals, while he is author of 10

chapters in medical books. He is Editor-in-Chief of the journal 'Hellenic Surgical Oncology', a reviewer for many international journals and a member of the Editorial Board of five international journals. He is a member of numerous international medical societies, mainly concerning surgical oncology, and a member of the Board of Directors of the Hellenic Society of Surgical Oncology. His topics of interest are surgical oncology in general, and more specifically melanoma, sarcoma, peritoneal carcinomatosis, hyperthermic intraperitoneal chemotherapy, ovarian, colorectal and breast cancer.



Thomas G. Maris (54 yrs) has worked as a Medical Physicist (a) at the Areteion University Hospital, Athens (1988–1998) and (b) at the University Hospital of Heraklion, Heraklion (1998–2003). Since 2003, he is an Assistant (2003) and Associate (2015) Professor of Medical Physics at the Medical School of the University of Crete. He is the author of 95 Medline peer reviewed publications (1657 non self-citations, h-index: 23, mean impact factor: 2.96) and 208 announcements in national (59) international (149) conferences/congresses. He has been given 40 invited lectures in Greece and Europe. He has been actively involved in 5 funded research projects (2 as a basic researcher and 3 as a project leader) with a total budget of 319.000 Euro. His research is focused on quantitative MRI techniques applied in the areas of basic research (MRI polymer gel dosimetry), and MRI clinical research (abdominal MRI, musculoskeletal MRI, MRI neuroimaging, MRI-hemosiderosis, MRI-osteoporosis). He is a national representative in the European Federation of Medical Physicists (EFOMP).

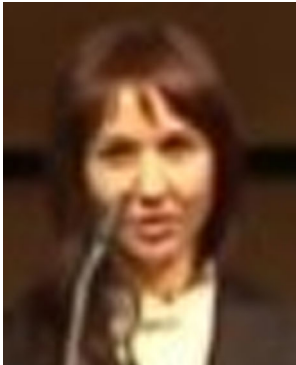


Dr. Apostolos Karantanas is Professor of Radiology - University of Crete, Chairman of the Department of Medical Imaging and Director of the Laboratory Section - Heraklion University Hospital, Member of the European Society of Radiology (ESOR) Programme Planning Committee, Member of the Educational Committee of European Society of Radiology (ESR), Member of the Sports Injuries Subcommittee/European Society musculoskeletal Radiology (ESSR), Affiliated Scientist to the FORTH-ICS institute and President of the Hellenic Society of Musculoskeletal Radiology. He is chairing the "Committee for Coordination of Academic Institutes" in Crete. Prof. Karantanas has given more than 500 invited lectures in 32 countries and is a regular faculty member in ESR, IDKD, International Skeletal Society,

Erasmus courses MSK MRI, School of MRI/ESMRMB, ESOR and ESSR. He is the author of 187 Medline/212 Scopus publications (h index 27, citations 2470; Google Scholar citations: 4150, h index:35, i10 index:100), 6 books, and 65 chapters in books. His main research is focused on imaging musculoskeletal disorders. He is associate editor in Hellenic Journal of Radiology and section editor in European Journal of Radiology. He is past President of ESSR and has chaired the ESSR annual meeting 2011 in Crete.



Eleftherios Kontopodis currently works as a Technical Staff member at the Computational BioMedicine Laboratory (CBML) in the medical image analysis field. He received his diploma from the National Technical University of Athens, school of Electrical and computer engineering with the specialization in Electronics and Systems after having also graduated from the department of Biomedical Engineering (Technological Educational Institute of Athens). Currently he is a PhD candidate at the Medical University of Crete. His research interests are in the areas of mathematical modeling and medical image processing.



Katerina Nikiforaki currently works as a technical staff member at the Computational BioMedicine Laboratory (CBML) in the medical image analysis field. Her MSc is in Medical Physics (University of Aberdeen, UK) and has background in Physics (University of Crete, Greece). She obtained working experience in the MRI field from the Radiology Dpt of Interbalkan Medical Center and continued as an application specialist for MRI scanners for a private company. Currently she is a PhD candidate at the Medical University of Crete. Her research areas are protocol optimization and medical image processing.



Kostas Marias is an Associate Professor in Image Processing at the Informatics Engineering Department of the Technological Educational Institute Of Crete and since 2010 he is the Head and Founder of the Computational Biomedicine Laboratory at FORTH-ICS (previously Biomedical Informatics Laboratory). Previously he was a Principal Researcher at the Institute of Computer Science (ICS-FORTH) since 2006. During 2000–2002, he worked as a Researcher at the University of Oxford and from 2003 to 2006 as Associated Researcher at FORTH-ICS. He was the coordinator two EC projects on cancer modelling (<http://www.contracancrum.eu/> and <http://www.tumor-project.eu/>), while during 2010–2015 actively participated in several other EC funded projects developing ICT technology focusing on medical image processing and personalized medicine. He has published more than 150 papers in international journals, books and conference proceedings focusing on medical image analysis, biomedical informatics and modelling for personalized medicine.